buildings

MDPI

Article

An Investigation of Parameter Sensitivity and a Dynamic Analysis of Subsurface Storage Chambers Utilizing the Finite Difference Method

Hongming Luo [1], Shan Lin [2], Quanke Hu [2] and Miao Dong [2,*]

[1] State Key Laboratory of Geomechanics and Geotechnical Engineering, Institute of Rock and Soil Mechanics, Chinese Academy of Sciences, Wuhan 430071, China; hmluo@whrsm.ac.cn
[2] Key Laboratory of Urban Security and Disaster Engineering, Ministry of Education, Beijing University of Technology, Beijing 100124, China; linshan@bjut.edu.cn (S.L.); zeroandone911@emails.bjut.edu.cn (Q.H.)
* Correspondence: dongmiao@emails.bjut.edu.cn

Abstract: Underground compressed air energy storage chambers are a promising emerging energy storage technology with strict limitations relating to the stability of the surrounding rock. This study conducted displacement and plastic zone analyses during the excavation and stabilization phases of the chamber utilizing the finite difference method based on engineering data, demonstrating that the stability of salt rock can effectively withstand internal pressures ranging from 0 to 9 MPa, with an average of 15 mm in the *Z*-axis and 19.23 mm in the *X*-axis. To further investigate the feasibility of subterranean energy storage reservoirs, the FOS for various surrounding rocks was calculated at different burial depths. These results facilitated a parameter sensitivity analysis on the stability of the surrounding rock of the underground energy storage reservoir. The dynamic reaction of the underground chamber was studied using synthetic seismic wave technology, demonstrating that the seismic capacity of the structure adhered to the code, and the post-seismic displacement remained within the safe range (*Z*-axis 34 mm, horizontal 19 mm). The results demonstrate the stability analysis method of the chamber and establish a foundation for the extensive implementation of CAES which will contribute to the development of energy storage technology.

Keywords: CAES; underground chamber; dynamic analysis; sensitivity study; FLAC3D; finite difference method; FOS; energy storage; geotechnical engineering

check for updates

Citation: Luo, H.; Lin, S.; Hu, Q.; Dong, M. An Investigation of Parameter Sensitivity and a Dynamic Analysis of Subsurface Storage Chambers Utilizing the Finite Difference Method. *Buildings* **2024**, *14*, 3778. https://doi.org/10.3390/buildings14123778

Academic Editors: Eugeniusz Koda and Yi Xue

Received: 24 October 2024
Revised: 21 November 2024
Accepted: 25 November 2024
Published: 26 November 2024

Copyright: © 2024 by the authors. Licensee MDPI, Basel, Switzerland. This article is an open access article distributed under the terms and conditions of the Creative Commons Attribution (CC BY) license (https://creativecommons.org/licenses/by/4.0/).

1. Introduction

Compressed air energy storage (CAES) technology is an innovative large-scale energy storage solution that effectively addresses the challenges of power system peak shaving and the temporal and spatial discrepancies in energy utilization [1]. In the context of the global advocacy for carbon neutrality and the reduction of energy consumption and emissions, the environmental protection benefits of compressed air subsurface energy storage chambers are especially significant [2]. Unlike traditional coal or gas power plants, CAES systems produce nearly zero direct CO_2 emissions. Although a minimal quantity of natural gas may be necessary for heating during the release of compressed air, the total carbon emissions are significantly lower than those from fossil fuel power generation. Furthermore, the energy storage medium (air) is ecologically sustainable and regenerative, generating neither waste nor pollution as chemical batteries do [3]. CAES utilizes compressed air as a medium for storing surplus energy, primarily to manage power fluctuations and enhance power quality. The primary components of a CAES power plant consist of compression, gas injection, and heat exchange systems, and storage apparatus [4]. This technology utilizes subterranean geological formations, such as caves, caverns, or salt caverns, to store substantial quantities of compressed air. The objective is to compress and store air underground via the compressor during periods of low power demand and surplus supply. During periods of elevated power

demand and inadequate supply, compressed air is discharged to activate the turbine for electricity generation, therefore balancing the grid load and enhancing energy efficiency [5].

The operational principle of compressed air subterranean energy storage consists of two primary stages: the charge phase and the discharge phase [6]. During periods of low electricity demand, such as the night-time or during peak wind and solar generation, a power surplus typically exists. Concurrently, the surplus electricity in the grid powers a compressor that extracts and compresses atmospheric air. Compressed high-pressure air is held in designated geological formations underground, such as constructed excavation chambers, natural caves, or salt caverns [7]. Due to their typical subterranean location, these geological formations possess excellent sealing and pressure-bearing capabilities, enabling them to endure and to retain substantial quantities of compressed air. This process equates to the transformation of electrical energy into the internal energy of air. Upon the arrival of peak power demand, the stored compressed air is discharged. During the release process, compressed air is initially heated through preheating or by combusting a small quantity of natural gas to elevate the temperature and pressure of the air, subsequently driving a turbine to produce energy. This process transforms the internal energy of compressed air into mechanical energy, which is subsequently turned into electrical energy and reintegrated into the grid to satisfy electricity demand. The expansion of compressed air upon release can propel the turbine, facilitating continuous electricity generation for a limited duration [7].

Compared with other energy storage technologies, the compressed air underground storage chamber has several significant advantages. Firstly, its energy storage scale can be very large, which is suitable for power grid peak shaving at a national or regional level. Due to the huge volume of the underground chamber, it can store large amounts of compressed air, which means that it is able to provide long-term power output, lasting for hours or even days, to meet large-scale electricity demand. Secondly, CAES can effectively balance the load of the grid, especially during peak consumption hours. By storing excess energy during power demand troughs and releasing this energy during peak demand hours, CAES can help grid operators alleviate power supply tightness and avoid blackouts, voltage fluctuations, and other energy supply problems. The application of this technology can significantly improve the reliability and flexibility of the power grid [8].

Compressed air storage facilities are mainly divided into ground gas storage tanks and underground gas storage. Considering factors such as cost and application scale, the practical application of underground gas storage is more extensive. Underground gas storage is mainly concentrated in abandoned or water-soluble underground salt caverns, abandoned underground mine tunnels [9,10]. The first three need to meet specific geological conditions, but suitable geological conditions may not be found in some areas, which limits their wide promotion and application. Therefore, when there is a lack of suitable geological conditions in the area, the site selection of a more flexible rock lining chamber is a better choice.

Full-size CAES systems are in operation in Germany (Huntorf CAES plant) and the United States (McIntosh CAES plant) [11], and the Huntorf plant in Germany [12], one of the pioneers in the application of CAES technology, is representative of the successful experience in utilizing salt caverns as an underground gas storage reservoir [13]. During its long-term operation, Huntorf Power Station has accumulated a huge amount of data, covering the mechanical response of salt rock under different pressure conditions, deformation characteristics, and long-term stability monitoring results, etc. These data are useful for the in-depth study of salt rock geology. These data provide a reference for the in-depth study of the characteristics of CAES system under the geological conditions of salt rock. The McIntosh Power Station in the United States is in the hard rock geologic area, and it has shown a series of innovative design and construction methods when facing the challenges of granite geologic conditions [14]. In the design of the underground gas storage facility, unique support structures and excavation methods were used to address the significant impact of granite joint fractures on stability. A salt rock gas storage project in a region of China incorporates the rich salt rock resources and specific geological conditions of the area. The engineering feasibility of this underground gas storage reservoir was analyzed [15].

The underground storage chamber has the characteristics of high internal pressure. During the compressed air storage process, high-pressure air generates significant pressure [16]. Since the overlying rock mass is unstable, it may result in rock rupture, collapse, or even ground subsidence, hence jeopardizing the safe operation of energy storage facilities [17,18]. The stability of the overlying rock mass is particularly important in areas with frequent crustal movement and seismic activity [19]. A robust rock mass can endure these high-pressure conditions for an extended duration, guaranteeing the reliable functioning of the energy storage system for decades or more. Conversely, unstable rock formations progressively diminish in stability under prolonged high pressure, potentially resulting in diminished system performance and heightened maintenance costs and operating risks. Consequently, analyzing the stability of the overlying rock mass is crucial. This work focuses on tunnel-type subterranean gas storage chambers. The research findings possess significant engineering applicability for assessing and verifying the burial depth of the subterranean rock-liner chamber during the initial feasibility study phase of the tunnel-type compressed gas energy storage power station.

In the field of geotechnical engineering, the finite difference method is a powerful numerical technique. It discretizes the governing equations of a physical problem into a set of difference equations [20]. By dividing the domain into a grid and approximating derivatives with finite differences, it enables the solution of complex problems such as the stability analysis of underground storage chambers. This method has been widely adopted due to its ability to handle nonlinear and heterogeneous materials, providing accurate predictions of the mechanical behavior and stability of geotechnical structures [21]. In this study, the results were verified through comparative analysis with prior research, benchmarking against established standards, and correlating with available field data, ensuring its accuracy and reliability in representing the physical system of the underground storage chamber.

The rest of this paper is structured as follows: Section 2 describes in detail the simulation techniques used in this study. Section 3 analyzes the static analysis results of the underground storage chamber and the sensitivity study of the parameters. Section 4 analyzes the dynamic response process of the chamber through synthetic seismic waves. In Section 5, the conclusion is given. The flowchart of this study is shown in Figure 1.

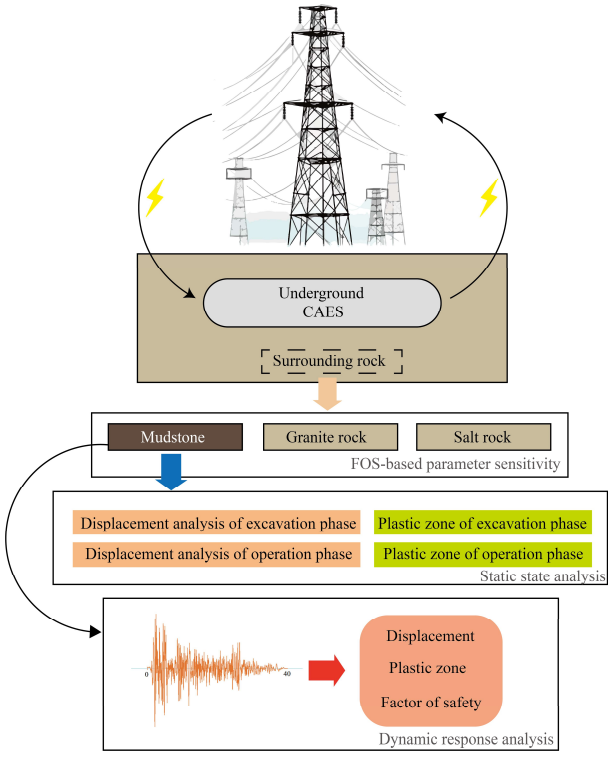


Figure 1. Flow chart of CAES surrounding rock analysis.

2. Method

2.1. Constitutive Model

In the analysis of subterranean structures, the material characteristics of soil and concrete are markedly distinct, necessitating the use of varied mechanical models to represent their various mechanical properties correctly [22].

Soil is a quintessential nonlinear material, and its mechanical behavior is influenced by numerous elements, including stress history, water content, density, and structure [23,24]. It will deform and fail when the stress attains a specific threshold. The Mohr–Coulomb criterion has been validated across numerous engineering applications [25], particularly in slope stability [26], tunnel design [27], and foundation-bearing capacity analysis. It utilizes cohesive force (c) and internal friction angle (φ) derived from soil properties, accounting for the frictional and cohesive characteristics of various soil types, including sand, clay, and gravel, thereby providing a more precise representation of soil strength characteristics. It effectively simulates soil yield behavior and demonstrates excellent reliability and practicality [28]. In this study, it was found that the predominantly slightly weathered calcareous silty mudstone underground rock formation behaved as a homogeneous material. Given the formation's uniform nature, the Mohr–Coulomb constitutive model was selected due to its capability to accurately represent the mechanical behavior of soil and rock in this context [29].

The main stress is used to represent the Mohr–Coulomb criterion in FLAC3D [30,31], where σ_1, σ_2, and σ_3 are the stress components in three directions in the 3D model. The directions are determined according to $\sigma_1 \leq \sigma_2 \leq \sigma_3$, and the corresponding strain components are ϵ_1, ϵ_2, and ϵ_3. The M–C criterion is represented in the $\sigma_1\sigma_2$ plane in Figure 2.

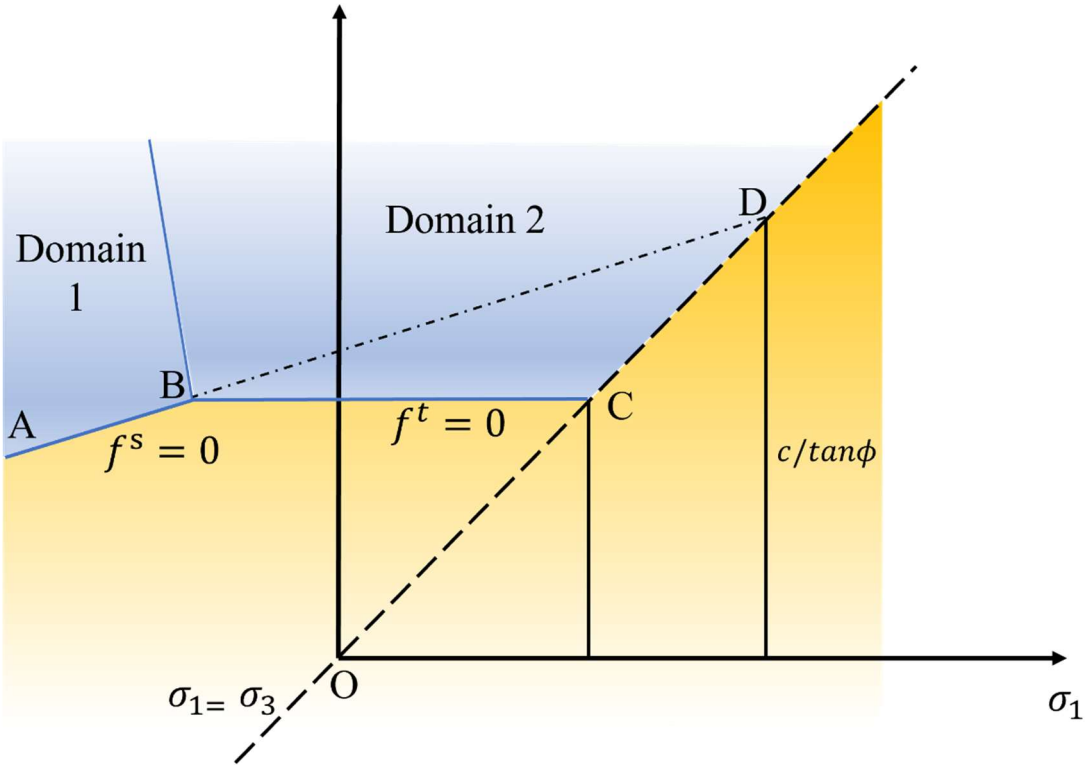


Figure 2. Schematic representation of the M–C criterion in the $\sigma_1\sigma_2$ plane.

Here, ϕ is the internal friction angle of the soil, c is the cohesive of the soil, the remaining parameters in the figure are given in Equations (1)–(3), and σ_t is tensile strength. $\sigma_{tmax} = c/tan\phi$

$$N_\phi = \frac{1 + \sin(\phi)}{1 - \sin(\phi)} \quad (1)$$

$$f^s = -\sigma_1 + \sigma_3 N_\phi - 2c\sqrt{N_\phi} \tag{2}$$

$$f^t = \sigma_3 - \sigma_t \tag{3}$$

During this iteration, when the stress point $\sigma_i^I (i = 1, 2, 3)$ is located in domain 1 above the failure envelope, shear failure occurs, ψ is the expansion angle, and the new stress component σ_i^N is determined by Equations (4) and (5). When located in domain 2, the soil undergoes tensile failure, and the stress component $\sigma_i^N = \sigma_t$. When the stress point is below the envelope, that is, the yellow area, then the soil does not fail at this time, and the stress component is still σ_i^I.

$$\begin{gathered} N_\psi = \frac{1+\sin(\psi)}{1-\sin(\psi)} \\ \sigma_1^N = \sigma_1^I + \lambda^s(\alpha_1 - \alpha_2 N_\psi) \\ \sigma_2^N = \sigma_2^I + \lambda^s \alpha_2 (1 - N_\psi) \\ \sigma_3^N = \sigma_3^I + \lambda^s(-\alpha_1 N_\psi + \alpha_2) \end{gathered} \tag{4}$$

$$\lambda^s = \frac{f^s(\sigma_1^I, \sigma_3^I)}{(\alpha_1 - \alpha_2 N_\psi) - (-\alpha_1 N_\psi + \alpha_2) N_\phi} \tag{5}$$

The stress–strain relationship of concrete is nearly linear in the interaction between the soil and supporting structure until it attains the yield point. A basic, isotropic linear elastic model can characterize the mechanical behavior at this point. In this study, the Mohr–Coulomb model is used for the surrounding rock, while the elastic model is utilized for the concrete support structure.

2.2. Factor of Safety

In order to express the stability of the underground storage chamber more clearly and intuitively, the Factor of Safety (FOS) is used to analyze the state of surrounding rock when the chamber works stably [32]. The FOS represents the ratio of the maximum load the structure can bear to the actual load and is calculated using strength reduction, which can be applied to basically any failure model by gradually reducing the shear strength of the material to reach the ultimate equilibrium state. In FLAC3D, firstly, a characteristic response time (N_r) is automatically found, and the cohesion and friction strength are set to larger values, so that the internal stress in the soil increases. In the process of continuous iteration, if the time step required for calculation exceeds N_r, the calculation will stop, and the FOS does not meet the requirements at this time. The reduction process of cohesion and internal friction angle is shown in Equations (6) and (7).

$$c^{\text{trial}} = \frac{1}{F^{\text{trial}}} c \tag{6}$$

$$\phi^{\text{trial}} = \arctan\left(\frac{1}{F^{\text{trial}}} \tan\phi\right) \tag{7}$$

2.3. Synthetic Seismic Waves

In the process of dynamic analysis in this study, an El-Centro synthetic seismic wave [33] is used to better simulate the real earthquake situation. According to the geographical location of the tunnel, the simulated seismic fortification intensity is 8 degrees, the designed basic seismic acceleration is 0.2 g, and the seismic waveform is shown in Figure 3.

In the finite difference simulation analysis, the seismic force is usually inputted by applying dynamic load at a boundary or an internal node, and the dynamic load is determined by using the acceleration time history, velocity time history, force time history, and stress time history. In order to ensure the function of the viscous constraint boundary, it is necessary to input the seismic wave in the way of the stress time history distribution in the dynamic analysis. The seismic wave distributed in the acceleration time history

is transformed into the velocity time history ν_s, ν_n, and then the velocity time history is transformed into the stress time history σ_s, σ_n. The seismic load can be successfully applied to the model and the integrity of the boundary characteristics can be ensured by using the chart input at the bottom boundary of the model [34].

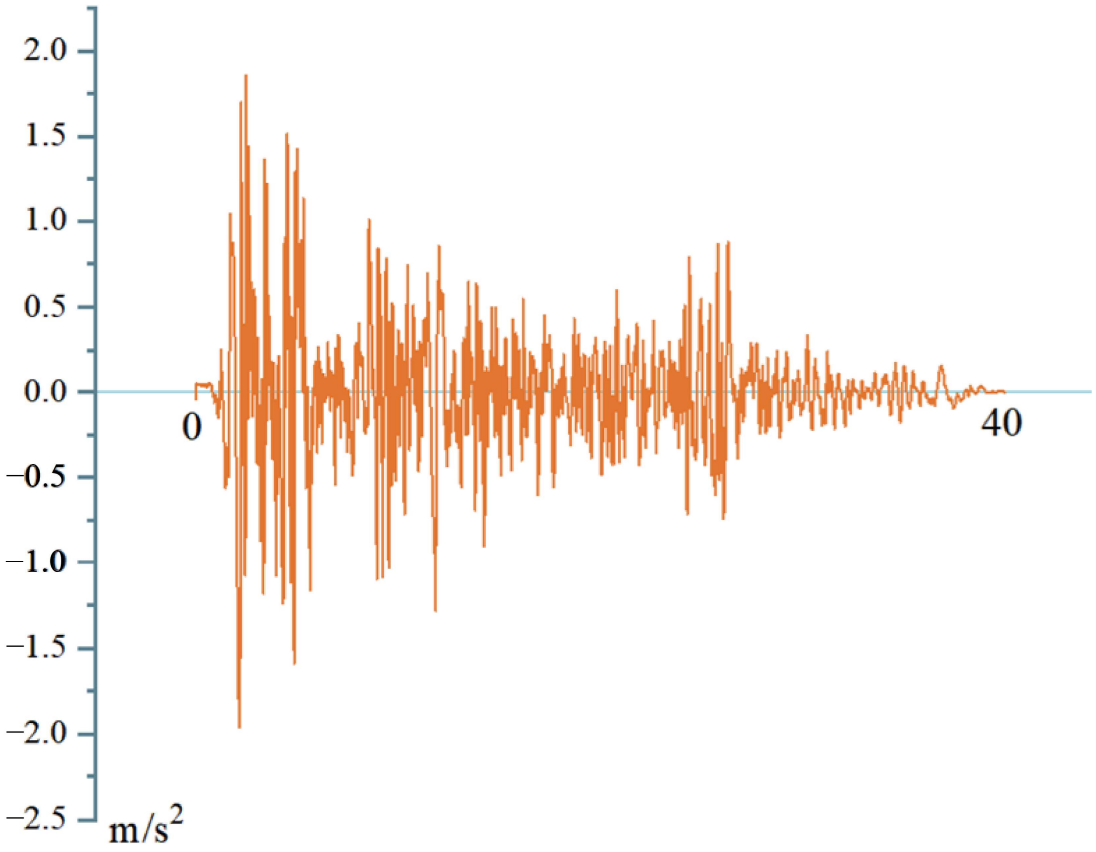


Figure 3. El-Centro synthetic seismic wave.

The particle velocities ν_s and ν_n in tangential and normal directions are transformed into stresses σ_s, σ_n, which is denoted by Equation (8).

$$\begin{aligned} \sigma_s &= -2(\rho \cdot C_s)\nu_s \\ \sigma_s &= -2(\rho \cdot C_n)\nu_n \end{aligned} \tag{8}$$

where ρ is the density of the medium, kg/m^3, and C_s, C_n are the wave velocities of the S wave and P wave of the medium, respectively.

2.4. Boundary Conditions

The Lagrangian difference method [35] was used to simulate the dynamic response under seismic action, and the coupling boundary conditions of free field boundary and viscous damper were used. A static boundary is set at the bottom of the model, and a free field boundary grid is generated around the model, so that the unbalanced force is applied to the boundary of the main grid, and the vibration wave is reflected back to the main structure. The critical minimum damping ratio was set to 0.03 and the minimum center frequency of Rayleigh damping was set to 1.0 Hz in the model. The dynamic boundary is shown in Figure 4.

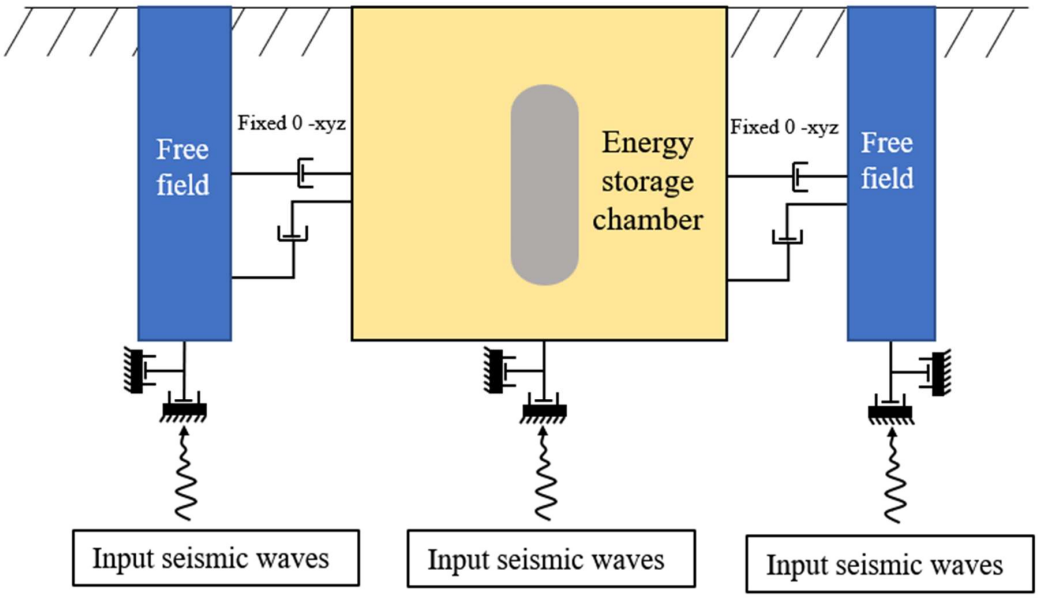


Figure 4. Schematic representation of the dynamic boundary of the seismic response.

3. Static Analysis Results

3.1. Engineering Project Introduction

The projected dimensions of the subterranean sealing chamber are 100,000 cubic meters, with a maximum operational internal pressure ranging from 4 to 9 MPa. It is situated 150 m below the surface. The primary project is situated on the northern slope of a mountain in a province in northwest China, encompassing around 100,000 square meters. There are nine Holocene active faults in the region, one late Pleistocene active fault in the proximal area, and no development of Holocene active faults. The engineering sector is situated inside a seismic zone, where significant and intense earthquakes have historically occurred with frequency. Numerous earthquakes exceeding magnitude VII have occurred, with a chance surpassing 10% within a 50-year timeframe. The maximum acceleration of bedrock ground motion is 0.2 g, equal to a seismic intensity of VIII, indicating poor regional structural stability.

3.2. Soil Information

During the initial phase of geological exploration for the project, drilling results at depths of 150 to 200 m indicate that the surrounding rock of the tunnel section predominantly consists of breeze calcarine silty mudstone, with minor inclusions of breeze morl and breeze siltstone, and the rock mass appears relatively intact. Information regarding the mudstone soil layer is presented in Table 1. The tunnel chamber section is chosen to replicate the two-dimensional plane at the straight segment of the tunnel in the project, with calculations based on the plane strain model. A unit length of 1 m is adopted. The model's left and right boundaries are restricted by normal displacement along the *X*-axis, while the bottom boundary is confined by displacement in the *Z*-axis direction, with the surface functioning as a free boundary. Based on the theoretical analysis of rock mechanics and results from the engineering field test, the Mohr–Coulomb model is chosen for the surrounding rock, while the elastic model is selected for the support and lining structure. The bulk modulus and shear modulus characterize the deformation modulus and Poisson's ratio of the adjacent rock and soil, as seen in Equations (9) and (10).

$$K = \frac{E}{3 \times (1 - 2\nu)} \tag{9}$$

$$G = \frac{E}{2 \times (1 + \nu)} \tag{10}$$

Table 1. Mudstone soil layer information.

Unit Weight (kN/m^2)	Deformation Modulus (Gpa)	Poisson's Ratio (μ)	Cohesive Forces (kpa)	Angle of Internal Friction (°)	Saturated Uniaxial Compressive Strength (Mpa)	Saturated Splitting Compressive Strength (Mpa)
25.8	6	0.25	500	40	22.09	3.53

3.3. Support Structure Information

During the excavation of the chamber, the initial support entirely withstands the surrounding rock pressure of the layer containing the gas storage chamber, but the secondary lining is not designed to handle this pressure. During the stable operational phase, the gas storage chamber can accommodate a working pressure range of 0.1 to 9 MPa, utilizing compressed air as the gas medium, with minimal water and oil content. The secondary lining primarily functions to convey the high-pressure gas within the chamber to the adjacent rock formations. Table 2 presents the structural details of the major support and secondary lining.

Table 2. The structural information of primary support and secondary lining.

Option	Concrete Material	Technology	Chamber Depth (m)	Thickness (m)
Primary support	C25	Shotcrete	150	0.15
Secondary lining	C40	Concreting	150	0.45

3.4. Static Analysis Result

Following the stabilization of the initial ground stress field, the stress relief and deformation are examined by the simulation of chamber excavation, and the preliminary support model is developed. The displacement cloud map (Figures 5 and 6) of the excavation phase illustrates the displacement distribution along the *X*-axis and *Z*-axis of the circular section.

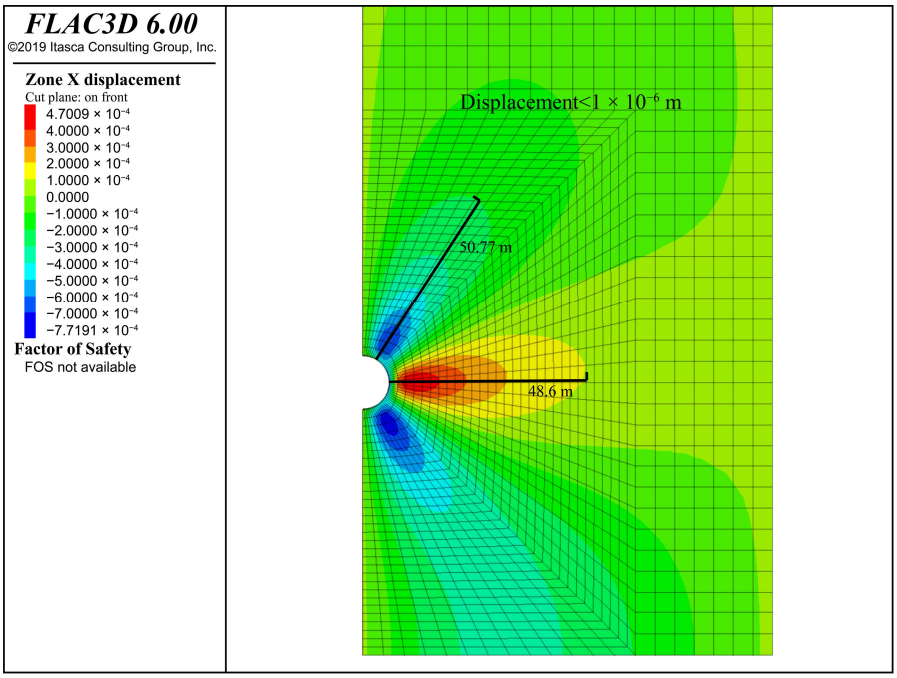


Figure 5. *X*-axis displacement cloud map of excavation stage.

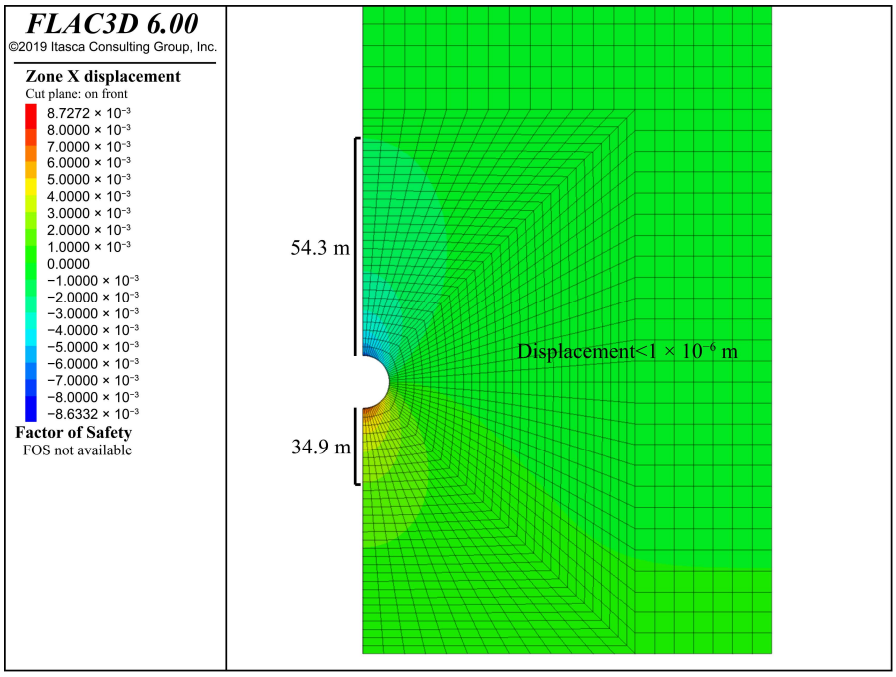


Figure 6. *Z*-axis displacement cloud map of excavation stage.

The displacement cloud map can be utilized to ascertain the deformation of the surrounding rock during cave excavation. The findings indicate that the settlement at the higher end of the circular section is 8.633 mm, the settlement at the lower end is 8.727 mm, and the horizontal expansion measures 0.470 mm during the excavation phase.

The plastic zone denotes the area where a material experiences plastic deformation under certain stress circumstances, as determined by its stress–strain properties. The varying geological conditions result in the distinct mechanical properties and deformation characteristics of the surrounding rock during the chamber construction [36]. In rock mechanics, the surrounding rock can be divided into elastic, elastic–plastic and plastic zones according to the strength and strain properties of the surrounding rock [37]. The plastic zone denotes the region where the material experiences permanent deformation upon surpassing the strength threshold during stress application. It may result in the failure of the surrounding rock and the deformation of the tunnel structure. Consequently, during the design and construction of the chamber, it is imperative to thoroughly analyze and assess the plastic zone of the surrounding rock to guarantee the stability and safety of the building. Figure 7 illustrates the distribution of the plastic zone during the chamber excavation phase. At this stage, plastic failure is confined to the periphery of the initial supporting structure, extending 2 m, while the surrounding rock remains largely undamaged and in a stable condition.

During the stable operation phase, the inner wall of the chamber withstands a maximum air pressure of 9 MPa. The simulation applies a normal pressure of 10 MPa to the inner wall of the chamber, and the deformation is investigated under stable limit operating conditions. The displacement cloud diagram (shown in Figures 8 and 9) depicts the displacement distribution of various section shapes under stable operation conditions.

The displacement cloud map reveals the deformation of surrounding rock under stable working conditions in each segment of the chamber. The findings indicate that during the stable operational phase, the upper extremity of the circular section experiences a settlement of 36.432 mm, the lower extremity settles by 31.923 mm, and the horizontal dimension expands by 19.703 mm, exhibiting little deformation in all directions.

The stable operational phase of the chamber reveals the distribution of the plastic zone, as illustrated in the Figure 10. It is evident that, due to air pressure, the extent of the plastic zone is significantly enlarged, predominantly along the Z-axis, extending 30 m upward

and 25 m downward. Furthermore, an analysis of the chamber's burial depth indicates that the plastic flow along the Z-axis is constrained to five times the chamber's diameter. The current FOS is 4.67, indicating a secure condition. The variation of the internal pressure within the range of 0–9 MPa has a profound impact on the mechanical behavior of the underground storage chamber. As the internal pressure increases, the displacement of the chamber structure, especially in the Z-axis direction, exhibits a significant upward trend. For instance, at an operational pressure of 10 MPa, the upper settlement reaches 36.43 mm and the lower settlement is 31.92 mm. This indicates that in the design of CAES systems, the structural integrity and material strength of the chamber must be carefully designed to withstand such deformations.

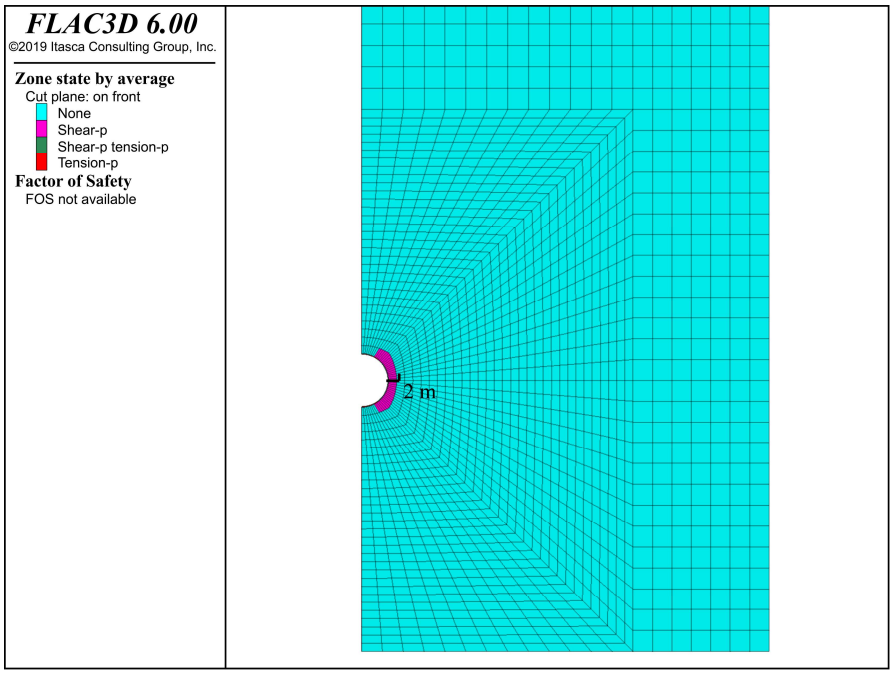


Figure 7. Plastic zone of surrounding rock in excavation stage.

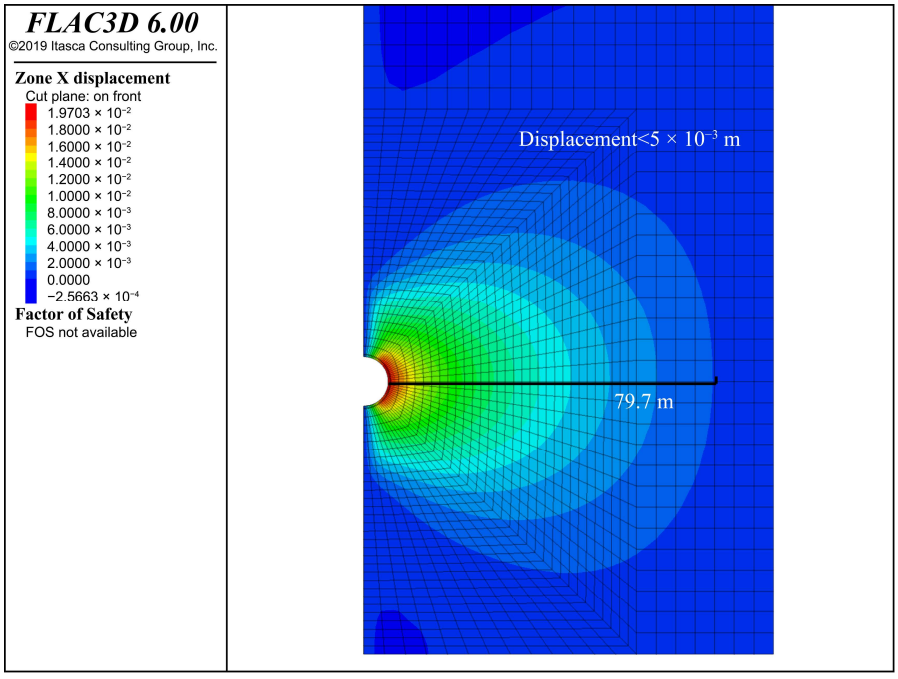


Figure 8. *X*-axis displacement cloud diagram of stable operation phase.

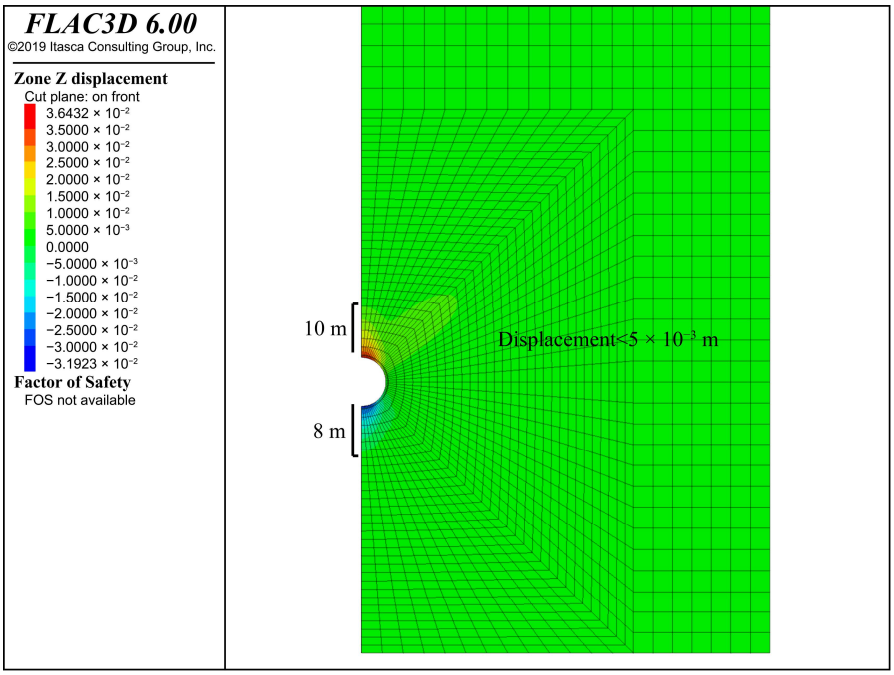


Figure 9. *Z*-axis displacement cloud diagram of stable operation phase.

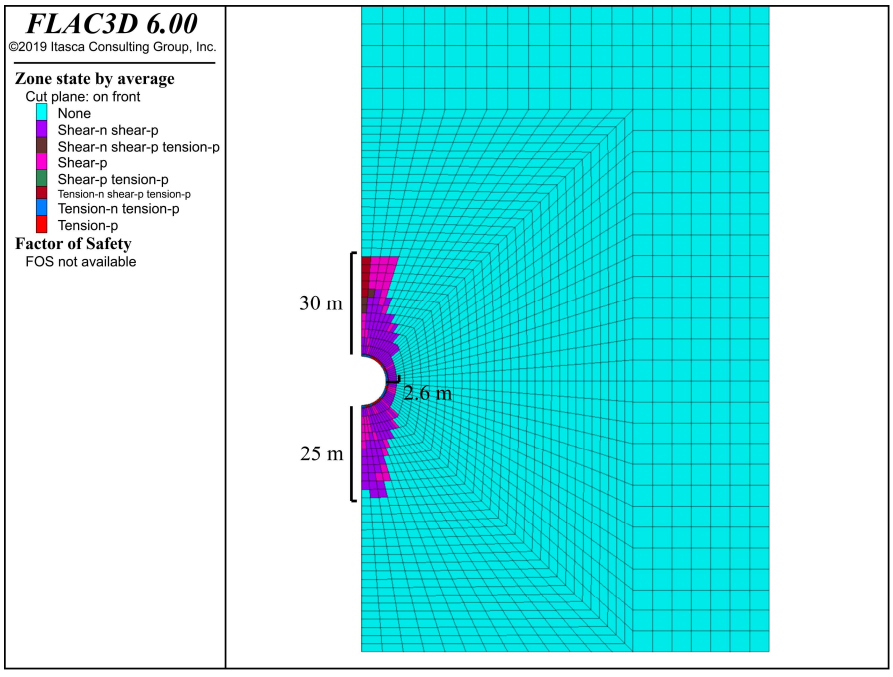


Figure 10. Plastic zone of surrounding rock in stable operation phase.

3.5. Parameter Sensitivity Study

In order to further study the stability of the underground storage chamber in the stable operation stage, in this study the granite surrounding rock and salt rock surrounding rock in a location in northern China are introduced to compare and analyze with this project under different burial depths and different pressure conditions. The geological conditions of the comparison group are shown in Table 3.

Table 3. Geological information characteristics of granites and salt rocks.

Soil Mass	Unit Weight (kN/m^2)	Poisson's Ratio (μ)	Cohesive Force (kpa)	Angle of Internal Friction (°)	Deformation Modulus (Gpa)	Bulk Modulus (Gpa)	Elastic Modulus (Gpa)
Granites	2650	0.25	2000	55	24	16	9.6
Salt	2200	0.3	450	40	4.5	3.75	1.73

When the chamber depth is 150 m, the FOS calculated according to the strength reduction method is shown in Table 4, and the line chart is shown in Figure 11.

Table 4. FOS of different soils under different chamber operating pressures at 150 m buried depth.

Depth of Burial (m)	Soil Mass	Storage Pressure (MPa)	FOS
150	Mudstone	10	4.67
		8	5.67
		6	6.15
	Granite rock	10	7.52
		8	7.82
		6	8.12
	Salt rock	10	0.998
		8	1.28
		6	2.65

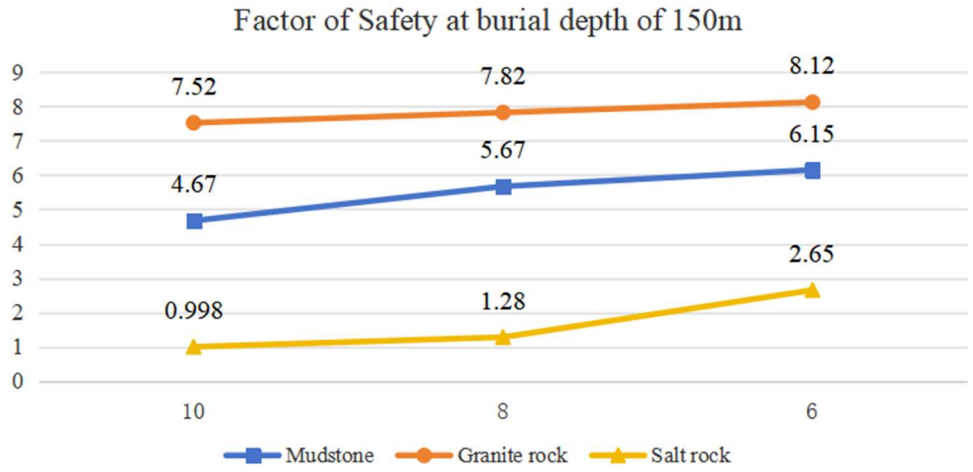


Figure 11. FOS at burial depth of 150 m.

When the chamber depth is 120 m, the FOS calculated according to the strength reduction method is shown in Table 5, and the line chart is shown in Figure 12.

Table 5. FOS of different soils under different chamber operating pressures at 120 m buried depth.

Depth of Burial (m)	Soil Mass	Storage Pressure (MPa)	FOS
120	Mudstone	10	2.21
		8	3.52
		6	5.98
	Granite rock	10	4.7
		8	6.02
		6	7.22
	Salt rock	10	0.82
		8	1.12
		6	3.82

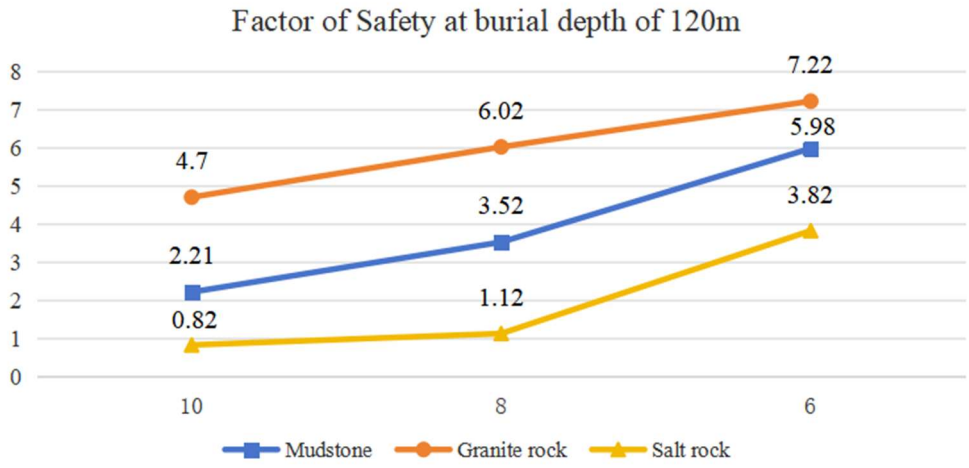


Figure 12. FOS at burial depth of 120 m.

When the depth of the chamber is 80 m, the FOS calculated according to the strength reduction method is shown in Table 6, and the line chart is shown in Figure 13.

Table 6. FOS of different soils under different chamber operating pressures at 80 m buried depth.

Depth of Burial (m)	Soil Mass	Storage Pressure (MPa)	FOS
80	Mudstone	10	1.871
		8	2.41
		6	3.45
	Granite rock	10	4.3
		8	5.45
		6	7.7
	Salt rock	10	0.78
		8	1.28
		6	2.65

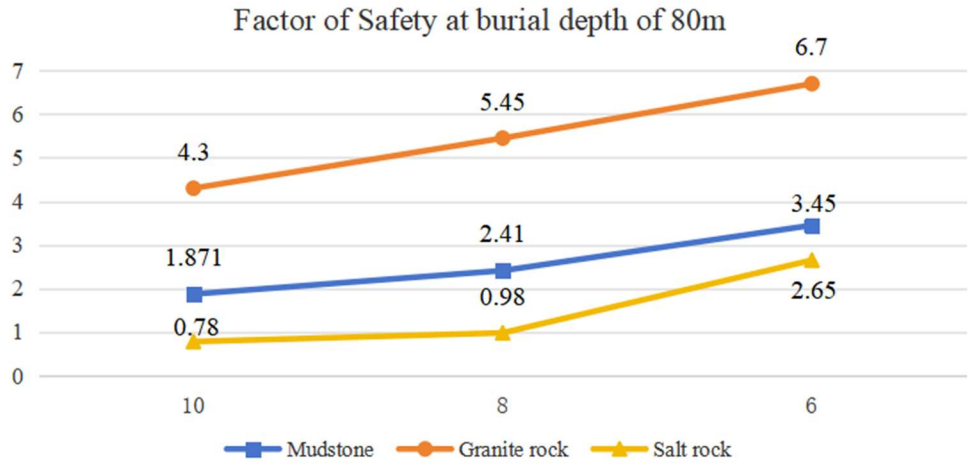


Figure 13. FOS at burial depth of 80 m.

According to the line chart analysis of pressure and buried depth, with the decrease in buried depth, the FOS of the surrounding rock is gradually increased, and the stability of the surrounding rock is improved. The FOS of salt rock under the three burial depths is less than 1, so it cannot be used as the surrounding rock of the storage chamber because it may lead to serious geological disasters. However, for granite and mudstone, the FOS is larger, but it still needs to be monitored during construction to prevent the occurrence of rock burst.

Since the FOS can simply quantify the stability degree of the surrounding rock, the change of the FOS represents the stability of the surrounding rock in the construction and operation process to avoid geological disasters such as landslides. In the design of underground engineering (such as tunnels, mines, etc.), the FOS of the surrounding rock is one of the important design bases. From the experimental results, it can be analyzed that for granite rock mass, due to its large rock stiffness, the change range of the FOS is also large. In the construction process, the requirements for the burial depth control are strict, otherwise the support structure needs to be changed significantly. However, the FOS of mudstone is relatively stable and is less affected by burial depth, and the control of burial depth is relatively loose for the same buried depth of the chamber. Since the bearing pressure range is 0–9 MPa, the surrounding rock needs to have better stability, so the selection of mudstone in the site selection of this project is more reasonable, which is of great significance to ensure the long-term stability and safety of the underground storage chamber. Previous research on underground storage technologies has shown that different geological formations impact stability and dynamic response. For granite, some studies reported high stability [38], similar to findings of a relatively high safety factor. Salt rock's instability in this study corroborates prior work [39]. Mudstone had a stable safety factor, consistent with previous emphasis on its properties. Overall, this study refines the understanding of different formations' behaviors in underground storage, providing a basis for future research and engineering applications.

In consideration of the influence of diverse geological conditions on the CAES system, this study presumed mudstone as the homogenous surrounding rock based on the ground investigation report. Additionally, preliminary analyses also assumed granite and salt rock. However, the complexity of actual geology far exceeds these simplified assumptions. Geological inhomogeneity is prevalent across all rock formations, and its impact on the stability and performance of underground gas storage should not be overlooked. The joints and fissures inherent in granite, the impurities and layered structures characteristic of salt rocks, and the variability in the properties of different layers of mudstones present numerous challenges to the operation of the CAES system. These challenges include localized stress concentrations, uneven settlement, and potential damage to structural integrity. In the future, further efforts will be directed towards exploring effective measures

to counteract these geologic inhomogeneities, thereby ensuring the stable operation of the system.

4. Dynamic Analysis Results

This selection of seismic parameters is in accordance with the relevant laws and regulations in China for seismic design. By using the maximum seismic grade of 0.2 g seismic wave at the project site, we aim to ensure that the dynamic analysis of the underground chamber is conducted under a realistic and safety-compliant seismic scenario. This allows us to evaluate the seismic response of the structure and determine its ability to withstand earthquakes in the region, providing a basis for assessing its seismic safety.

To assess the response and safety of underground gas storage chambers during seismic events, optimize the design to improve seismic resilience, and devise effective vibration mitigation strategies, thereby ensuring structural stability and safety during earthquakes while enhancing economic viability and sustainability, this study conducted a dynamic analysis of the chamber structure in a stable operational state (10 MPa) under mudstone geological settings. Figures 14 and 15 illustrate the displacement cloud image of the structure subjected to a high-frequency seismic condition of 25 Hz after 10 s.

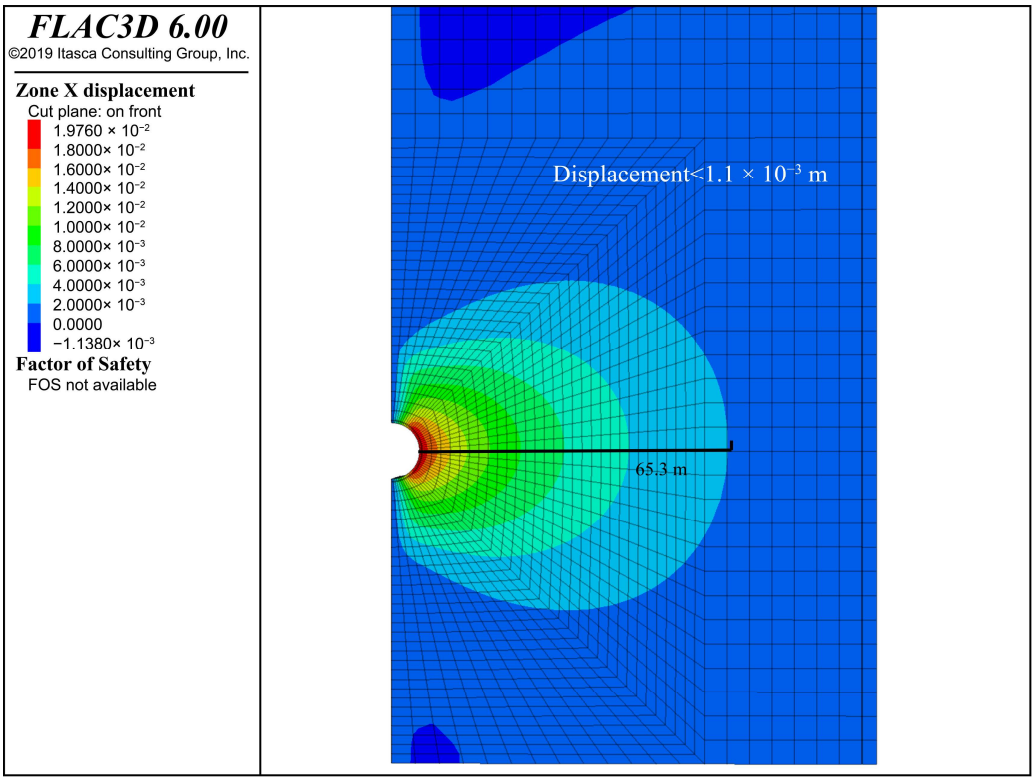


Figure 14. Seismic response *X*-axis displacement cloud map.

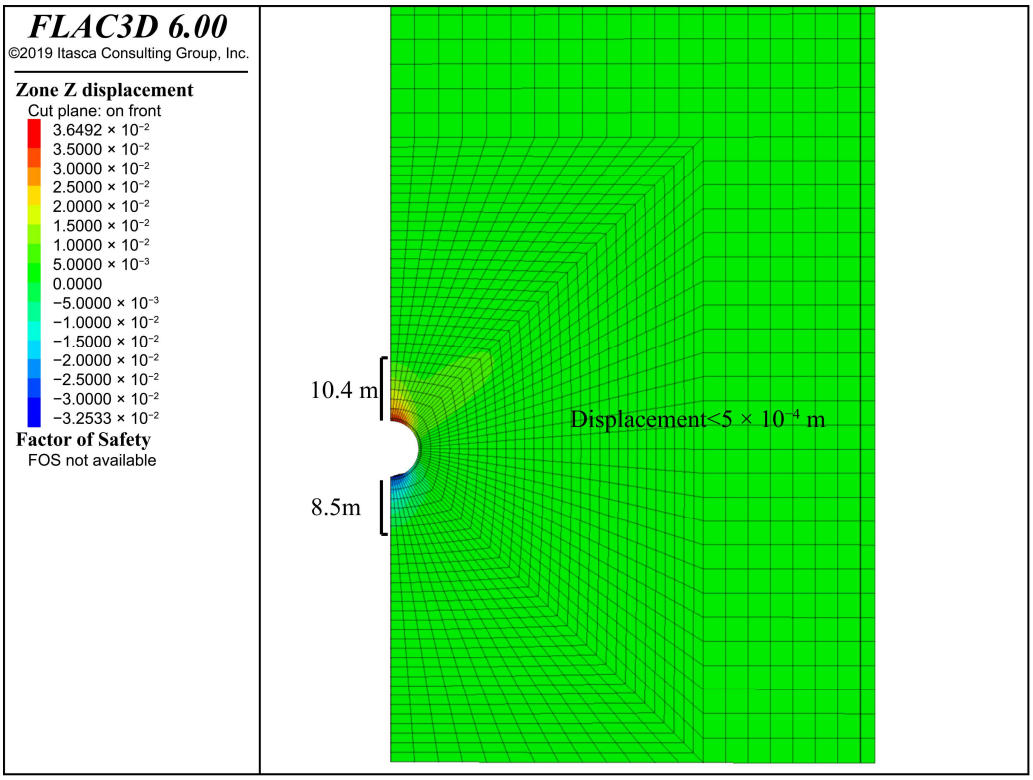


Figure 15. Seismic response *Z*-axis displacement cloud map.

It can be seen from the figure that the maximum displacement of the upper end of the chamber structure is 36.49 mm, the maximum displacement of the bottom is 32.53 mm, and the maximum displacement of the horizontal is 19.76 mm. Compared with the stable operation state, the roof settlement increased by 0.1%, the bottom settlement increased by 2%, and the horizontal expansion increased by 1%. According to the local historical earthquake level, the displacement was less than the standard value, and the structure was still in a safe state.

Figure 16 illustrates the displacement curve for each section of the chamber during the matching 10 s earthquake. The blue line represents the displacement curve of the chamber's farthest end along the *X*-axis, the red line denotes the displacement curve of the *X*-axis at the chamber's top, the green line illustrates the displacement curve of the farthest end along the *Z*-axis, and the yellow line indicates the displacement of the *Z*-axis at the chamber's top. The research indicates that the displacement of both the uppermost and the most distant horizontal sections have a specific periodicity, with an overall tendency resembling that of the input seismic wave. The seismic displacement of the most distant horizontal section is significantly greater than that of the upper section, whereas the seismic variation of the upper section is mostly influenced by the feedback effect of the soil and overlay. The chamber's horizontal end often experiences a more significant lateral impact from the earthquake, whereas the distal end encounters a more intense lateral force. Upon encountering the distal end of the chamber, the local seismic wave will concentrate energy at that location, resulting in significant displacement. In terms of *Z*-axis displacement, the seismic wave travels from the bottom to the top, causing a 0.1 s discrepancy in the maximum displacement timing between the top and the farthest horizontal end. In contrast to *X*-axis displacement, the seismic displacement at the farthest horizontal end of the *Z*-axis is less than the top displacement, which is more vulnerable to P and S waves due to the proximity of the chamber's top to the surface. The waves resulted in an elevation of vertical displacement at the chamber's top. For mudstone surrounding rock, the results of static analysis and dynamic analysis in this study are shown in Table 7.

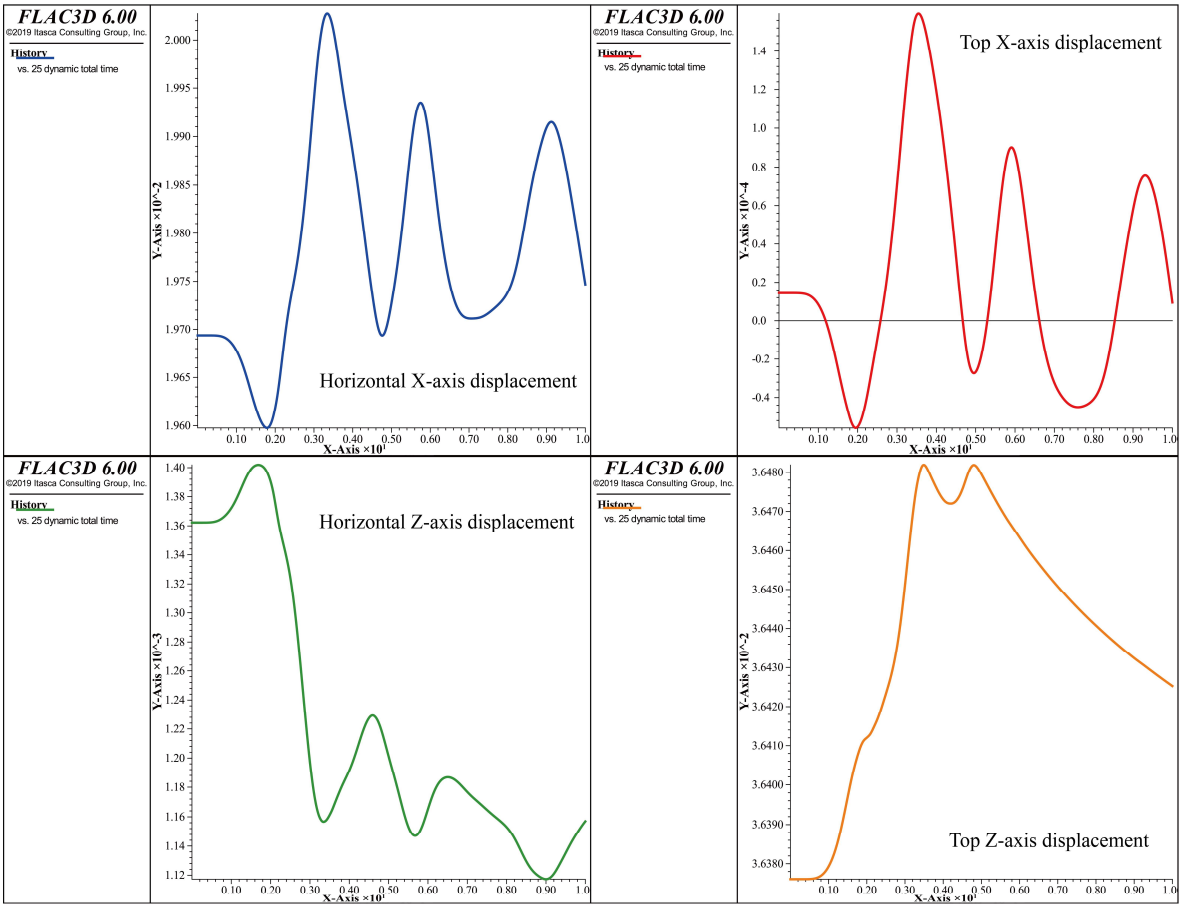


Figure 16. The displacement curve of each part of the chamber in a 10 s earthquake.

Table 7. Results of static and dynamic analysis of this project.

Analysis	Phase	Displacement (mm)			Plastic Zone (m^2)
		Top	Bottom	Horizontal	Approximate Area
Static	Excavation	8.633	8.727	0.470	35.184
	Stable	36.432	31.923	19.703	423.600
Dynamic		36.490	32.530	19.760	

5. Conclusions

This study selected three different geotechnical and geological scenarios from actual engineering projects to evaluate the stability of the underground CAES chamber's surrounding rock. The finite difference method and limit equilibrium method were used, along with a parameter sensitivity analysis considering actual engineering conditions. Authentic engineering data enhanced the simulation's effectiveness. FLAC3D was employed for explicit Lagrangian iterations and dynamic analysis. The key findings are as follows:

1. The static analysis outcomes of the excavation phase and stable operation phase of the underground storage chamber, utilizing the finite difference method, indicate that during the excavation phase the top settlement of the chamber measures 8.633 mm, the lower end settlement is 8.727 mm, and the outer expansion at the most distal horizontal end is 0.470 mm. The stress distribution is symmetrical, and the displacement remains within an acceptable range. At the operational limit of 10 MPa, the upper settlement of the chamber measures 36.43 mm, the lower settlement is 31.92 mm, and the maximum horizontal displacement is 19.70 mm. The deformation along the Z-axis is under one-thousandth of the burial depth, and the horizontal deformation along the X-axis

is below one percent of the chamber's diameter, indicating that the chamber structure is in a secure condition.

2. The simulation results of the plastic zone surrounding the rock indicate that during the excavation phase, a plastic zone emerges within a 2 m radius of the chamber structure. Following the transition to the stable operation phase, the plastic zone predominantly extends along the Z-axis, with an expansion range of up to 30 m, which is less than one-fifth of the burial depth, thereby ensuring the surrounding rock remains in a safe condition.
3. The safety factor of the surrounding rock of the underground storage chamber is analyzed by implementing the identical numerical simulation technique based on the other two actual geological circumstances. The results indicate that in the excavation and operation of rock masses with high stiffness, such as granite, the safety factor of the surrounding rock is maximized but exhibits significant variability with respect to the factors. Conversely, in mudstone rock masses, the safety factor remains more stable and has minimal fluctuations. The salt rock mass has the lowest safety factor, falling below 1 within the 8–10 MPa range, indicating considerable instability of the rock mass. The parameter research of chamber stability establishes the foundation for site selection in the actual project.
4. Under a 25 Hz, 0.2 g seismic acceleration wave, the upper end's maximum displacement was 36.49 mm, the bottom was 32.53 mm, and the post-earthquake maximum horizontal displacement was 19.76 mm. Compared with the stable operation state, the roof settlement increased by 0.1%, the bottom settlement by 2%, and the horizontal spread by 1%, demonstrating the structure's effective seismic capacity as the post-seismic displacement remained within the safe range.

In summary, this study comprehensively analyzed the displacement and stability of the underground CAES chamber in different phases, with a particular focus on the chamber's stability under various conditions and its seismic performance. The study demonstrates that the mudstone geological condition offers relatively good stability and a stable safety factor, making it suitable for the site selection of the underground storage chamber of the CAES system, though attention must be paid to the influence of internal pressure and burial depth. In contrast, the granite geological condition exhibits a relatively high safety factor but is sensitive to burial depth, necessitating strict control in design and construction. Conversely, the salt rock condition exhibits poor stability and requires special treatment or should be avoided altogether. These findings provide a reliable basis for engineering site selection and numerical simulation. Future research will focus on the development of more sophisticated numerical simulation models to improve the accuracy of prediction of underground CAES chamber behavior. At the same time, the joint information and failure mode of the rock will be further analyzed.

Author Contributions: Conceptualization, M.D. and H.L.; methodology, H.L.; software, S.L.; validation, S.L. and Q.H.; formal analysis, H.L.; writing—original draft preparation, H.L.; writing—review and editing, M.D.; visualization, Q.H.; supervision, S.L.; funding acquisition, S.L. All authors have read and agreed to the published version of the manuscript.

Funding: This research was funded by the Natural Science Foundation of China under grants no. 42107214, no. 42477157, and no. 42077270.

Data Availability Statement: Data will be made available on request.

Conflicts of Interest: The authors declare no conflicts of interest.

References

1. Sawyer, S.; Teske, S.; Fried, L.; Shukla, S. *Global Wind Energy Outlook 2016*. 2016. Available online: https://gwec.net/global-wind-energy-outlook-2016/ (accessed on 24 November 2024).
2. Erdemir, D.; Dincer, I. Development and assessment of a novel hydrogen storage unit combined with compressed air energy storage. *Appl. Therm. Eng.* **2023**, *219*, 119524. [CrossRef]

3. Finkenrath, M.; Pazzi, S.; D'Ercole, M.; Marquardt, R.; Moser, P.; Klafki, M.; Zunft, S. *Status and Technical Challenges of Compressed Air Energy Storage (CAES) Technology*. 2009. Available online: https://www.researchgate.net/publication/256091143_Status_and_Technical_Challenges_of_Compressed_Air_Energy_Storage_CAES_Technology (accessed on 24 November 2024).
4. Succar, S.; Williams, R.H. *Compressed Air Energy Storage: Theory, Resources, and Applications for Wind Power*; Princeton Environmental Institute: Princeton, NJ, USA, 2008.
5. Luo, X.; Wang, J.; Dooner, M.; Clarke, J. Overview of current development in electrical energy storage technologies and the application potential in power system operation. *Appl. Energy* **2015**, *137*, 511–536. [CrossRef]
6. Chen, H.; Cong, T.N.; Yang, W.; Tan, C.; Li, Y.; Ding, Y. Progress in electrical energy storage system: A critical review. *Prog. Nat. Sci.* **2009**, *19*, 291–312. [CrossRef]
7. Madlener, R.; Latz, J. Economics of centralized and decentralized compressed air energy storage for enhanced grid integration of wind power. *Appl. Energy* **2013**, *101*, 299–309. [CrossRef]
8. Du, T.Z.; Liu, X.; Shen, H.B.; Gu, Y.X.; Liu, L.S.; Wang, Z.Y. Performance study of a compressed air energy storage system incorporating abandoned oil wells as air storage tank. *Case Stud. Therm. Eng.* **2024**, *61*, 104776. [CrossRef]
9. Rutqvist, J.; Kim, H.-M.; Ryu, D.-W.; Synn, J.-H.; Song, W.-K. Modeling of coupled thermodynamic and geomechanical performance of underground compressed air energy storage in lined rock caverns. *Int. J. Rock Mech. Min. Sci.* **2012**, *52*, 71–81. [CrossRef]
10. Giramonti, A.J.; Smith, E.B.; Blecher, W.A.; Robson, F.L. *Compressed-air energy storage using hard-rock geology: Champagne effect model*; U.S. Department of Energy Office of Scientific and Technical Information: Washington, DC, USA, 1990.
11. Zhang, X.; Gao, Z.; Zhou, B.; Guo, H.; Xu, Y.; Ding, Y.; Chen, H. Advanced Compressed Air Energy Storage Systems: Fundamentals and Applications. *Engineering* **2024**, *34*, 246–269. [CrossRef]
12. Foley, A.; Díaz Lobera, I. Impacts of compressed air energy storage plant on an electricity market with a large renewable energy portfolio. *Energy* **2013**, *57*, 85–94. [CrossRef]
13. Mahlia, T.M.I.; Saktisahdan, T.J.; Jannifar, A.; Hasan, M.H.; Matseelar, H.S.C. A review of available methods and development on energy storage; technology update. *Renew. Sustain. Energy Rev.* **2014**, *33*, 532–545. [CrossRef]
14. Aghahosseini, A.; Breyer, C. Assessment of geological resource potential for compressed air energy storage in global electricity supply. *Energy Convers. Manag.* **2018**, *169*, 161–173. [CrossRef]
15. Li, H.; Ma, H.; Zhao, K.; Zhu, S.; Yang, K.; Zeng, Z.; Zheng, Z.; Yang, C. Parameter design of the compressed air energy storage salt cavern in highly impure rock salt formations. *Energy* **2024**, *286*, 129520. [CrossRef]
16. Jiang, F.; He, P.; Wang, G.; Zheng, C.C.; Xiao, Z.Y.; Wu, Y.; Lv, Z.H. Q-method optimization of tunnel surrounding rock classification by fuzzy reasoning model and support vector machine. *Soft Comput.* **2022**, *26*, 7545–7558. [CrossRef]
17. Raju, M.; Kumar Khaitan, S. Modeling and simulation of compressed air storage in caverns: A case study of the Huntorf plant. *Appl. Energy* **2012**, *89*, 474–481. [CrossRef]
18. Xia, C.; Zhou, Y.; Zhou, S.; Zhang, P.; Wang, F. A simplified and unified analytical solution for temperature and pressure variations in compressed air energy storage caverns. *Renew. Energy* **2015**, *74*, 718–726. [CrossRef]
19. Xiao, W.J.; Zhang, D.M.; Li, S.J.; Lu, J. Fracture evolution and fracture mechanism of tunnel surrounding rock: A case study based on laboratory tests and theoretical analysis. *Fatigue Fract. Eng. Mater. Struct.* **2023**, *46*, 2617–2638. [CrossRef]
20. Mu, R.Q.; Song, L.B.; Qin, Q.S. A meshless method based on the generalized finite difference method for 2D and 3D anisotropic elliptic interface problems. *Eng. Anal. Bound. Elem.* **2024**, *163*, 505–516. [CrossRef]
21. Watson, B.P.; Maphosa, T.J.; Roberts, D.P.; Gardner, L.J. Determination of strength of UG2 chromitite pillars at Impala Platinum from laboratory tests and FLAC3D. *J. South. Afr. Inst. Min. Metall.* **2024**, *124*, 437–446. [CrossRef]
22. Vásárhelyi, B.; Narimani, S.; Davarpanah, S.M.; Mocsár, G. Modeling Brittle-to-Ductile Transitions in Rock Masses: Integrating the Geological Strength Index with the Hoek–Brown Criterion. *Appl. Mech.* **2024**, *5*, 634–645. [CrossRef]
23. Xiang, G.S.; Ye, W.M.; Jalal, F.E. Shear strength of bentonite-sand mixture saturated with saline solution. *Environ. Earth Sci.* **2021**, *80*, 770. [CrossRef]
24. Lu, N.; Likos, W.J. Suction stress characteristic curve for unsaturated soil. *J. Geotech. Geoenviron. Eng.* **2006**, *132*, 131–142. [CrossRef]
25. Yang, S.Q.; Huang, Y.H. An experimental study on deformation and failure mechanical behavior of granite containing a single fissure under different confining pressures. *Environ. Earth Sci.* **2017**, *76*, 364. [CrossRef]
26. Chang, K.T.; Ge, L.; Lin, H.H. Slope creep behavior: Observations and simulations. *Environ. Earth Sci.* **2015**, *73*, 275–287. [CrossRef]
27. Liu, H.; Li, P.; Liu, J. Numerical investigation of underlying tunnel heave during a new tunnel construction. *Tunn. Undergr. Space Technol.* **2011**, *26*, 276–283. [CrossRef]
28. Harabinova, S.; Panulinova, E.; Kormanikova, E. Effect of Soil Material Models on the Prediction of Earth Embankment Deformations. In Proceedings of the International Conference on Numerical Analysis and Applied Mathematics (ICNAAM), Heraklion, Greece, 19–25 September 2022.
29. Melentijevic, S.; Berisavljevic, Z.; Berisavljevic, D.; Marañón, C.O. Rock slope stability analysis under Hoek-Brown failure criterion with different flow rules. *Bull. Eng. Geol. Environ.* **2024**, *83*, 181. [CrossRef]
30. Huang, J.; Han, J. 3D coupled mechanical and hydraulic modeling of a geosynthetic-reinforced deep mixed column-supported embankment. *Geotext. Geomembr.* **2009**, *27*, 272–280. [CrossRef]

31. Besharatinezhad, A.; Torok, A. Numerical simulation of P and S wave propagation in porous and low porosity carbonate rocks: Laboratory tests, automatic P and S waves detection and FLAC3D simulation. *Bull. Eng. Geol. Environ.* **2024**, *83*, 323. [CrossRef]
32. Chen, F.; Wang, L.; Zhang, W. Reliability assessment on stability of tunnelling perpendicularly beneath an existing tunnel considering spatial variabilities of rock mass properties. *Tunn. Undergr. Space Technol.* **2019**, *88*, 276–289. [CrossRef]
33. Hartzell, S.H. Earthquake aftershocks as Green's functions. *Geophys. Res. Lett.* **1978**, *5*, 1–4. [CrossRef]
34. Deng, T.F.; Gui, Y.; Nie, F.S. Comparative Analysis of Several Common Quasi-statics Methods for Tunnel Seismic Soil Pressure Calculation. In Proceedings of the 2nd International Conference on Civil Engineering, Architecture and Building Materials (CEABM 2012), Yantai, China, 25–27 May 2012; pp. 2253–2258.
35. Benmebarek, S.; Khelifa, T.; Benmebarek, N.; Kastner, R. Numerical evaluation of 3D passive earth pressure coefficients for retaining wall subjected to translation. *Comput. Geotech.* **2008**, *35*, 47–60. [CrossRef]
36. Jing, W.; Zhou, J.; Yuan, L.; Jin, R.C.; Jing, L.W. Deformation and Failure Mechanism of Surrounding Rock in Deep Soft Rock Tunnels Considering Rock Rheology and Different Strength Criteria. *Rock Mech. Rock Eng.* **2024**, *57*, 545–580. [CrossRef]
37. Zhu, Z.Q.; Sheng, Q.; Li, J.H. Elasto-plastic analysis of a circular opening considering material dilatancy and elasto-plastic coupling effects. *J. Chin. Inst. Eng.* **2018**, *41*, 239–246. [CrossRef]
38. Nadaf, M.B.; Maralapalle, V.; Zende, A.A.; Momin, A.I.A. Mineralogical composition and strength characteristics of granite rocks. *Sadhana-Acad. Proc. Eng. Sci.* **2024**, *49*, 287. [CrossRef]
39. Bauer, S.J.; Song, B.; Sanborn, B. Dynamic compressive strength of rock salts. *Int. J. Rock Mech. Min. Sci.* **2019**, *113*, 112–120. [CrossRef]

Disclaimer/Publisher's Note: The statements, opinions and data contained in all publications are solely those of the individual author(s) and contributor(s) and not of MDPI and/or the editor(s). MDPI and/or the editor(s) disclaim responsibility for any injury to people or property resulting from any ideas, methods, instructions or products referred to in the content.